LA-7941-MS

2

X-Ray Diodes for Laser Fusion Plasma Diagnostics

University of California

LOS ALAMOS SCIENTIFIC LABORATORY

Post Office Box 1663 Los Alamos, New Mexico 87545

UNITED STATES
DEPARTMENT OF ENERGY
CONTRACT W-7405-ENG. 36

LA-7941-MS

UC-21
Issued: February 1981

X-Ray Diodes for Laser Fusion Plasma Diagnostics

R. H. Day
P. Lee
E. B. Saloman*
D. J. Nagel**

---

*National Bureau of Standards, Washington, DC 20234.
**Naval Research Laboratory, X-Ray Optics Branch, Washington, DC 20375.

X-RAY DIODES FOR LASER FUSION PLASMA DIAGNOSTICS

by

R. H. Day, P. Lee, E. B. Saloman, and D. J. Nagel

ABSTRACT

Photodiodes with x-ray sensitive photocathodes are commonly used as broadband x-ray detectors in fusion plasma diagnostics. We have measured the risetime of the detector system and have measured the quantum efficiency between 1-500 Å of numerous photocathode materials of practical interest. The materials studied include aluminum, copper, nickel, gold, three forms of carbon, chromium, and cesium iodide. The results of the measurements are compared with Henke's semiempirical model of photoyield. We have studied the effects of long-term cathode aging and use as a plasma diagnostic on cathode quantum efficiency. In addition, we have measured the x-ray mass-absorption coefficient of several ultrasoft x-ray windows in energy regions where data were unavailable. Windows studied were made of aluminum, Formvar, polypropylene, and Kimfoil. Measurements between 1-50 Å were performed with the Los Alamos Scientific Laboratory's low-energy x-ray calibration facility, and the measurements between 50-550 Å were performed at the National Bureau of Standard's synchrotron ultraviolet radiation facility.

I. INTRODUCTION

In the laser fusion experimental program at the Los Alamos Scientific Laboratory (LASL), we use x-ray diagnostics as a primary means of monitoring the laser-target interaction and subsequent implosion. We measure temporally, spatially, and energy-resolved x rays from the high-temperature plasma. Although we never measure all of these parameters with a single instrument, we do sample a limited region of one or two of these variables with a single detector. Temporal resolution of laser fusion plasmas is particularly difficult, because the events occur as single pulses that last from a few tens of picoseconds to a nanosecond. To perform high-bandwidth energy-resolved x-ray measurements, we developed biplanar x-ray sensitive diodes whose signals are recorded with state-of-the-art high-speed oscilloscopes.

Biplanar diodes with x-ray sensitive photocathodes have been used as broadband x-ray detectors in several plasma diagnostics applications.[1,2] An x-ray diode (XRD) is shown in Fig. 1. It is a simple detector with a

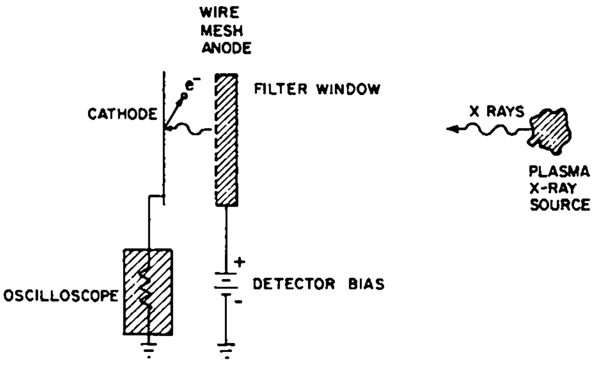

Fig. 1.
A biplanar XRD.

cathode that views the x-ray source through a filter window. The anode can be either the filter window, if it has a metallic surface, or a separate wire mesh placed between the window and the cathode.

The detector's energy-dependent response is determined by the photocathode's photoelectric quantum efficiency multiplied by the transmission of the filter window and anode. Typical response curves for an aluminum photocathode with various filter window anodes are shown in Fig. 2. The detector's temporal response is determined by its geometry and the bandwidth of the recording system. We built detectors with a 65-ps full width at half maximum (FWHM)[3] and recorded the signals on a 5-GHz bandwidth oscilloscope with a 150-mV/cm vertical sensitivity. The primary virtues of these detectors are their simplicity, speed, and cost while providing moderate energy resolution.

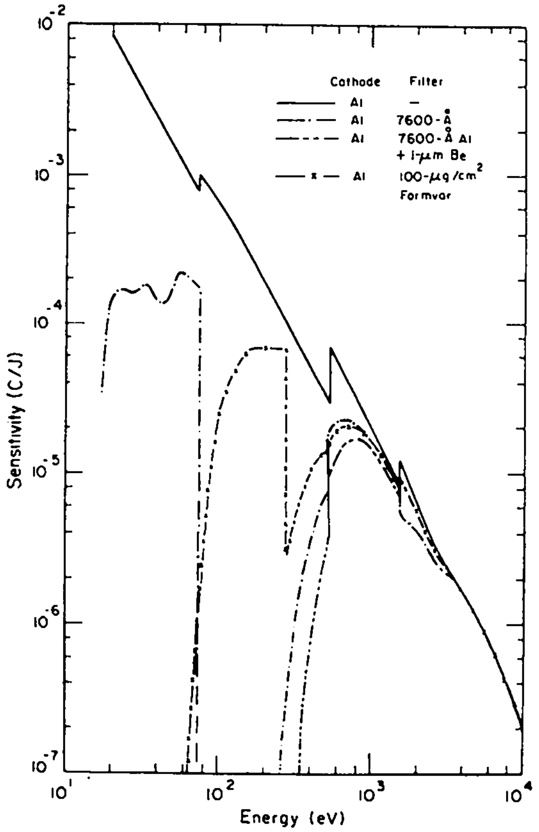

Fig. 2.
Response curve of an aluminum cathode convolved with several filter windows.

To make a useful detector system, it is necessary to know the quantum efficiency of the cathodes and transmission of the filter windows over the energy range of interest, which for us is 10 eV to 10 keV. Quantum efficiencies have been measured for many years, but relatively few data are available for cathode materials of practical interest over this extended energy range. Cairns and Samson[4] surveyed the photoelectric yields of 16 metallic photocathodes from 10 to 60 eV, Saloman[5] measured $Al_2 O_3$ from 25 to 250 eV, Gaines and Hansen[6] characterized gold from 1.5 to 8 keV, and Eliseenko et al.[7] measured a number of metallic and dielectric photocathodes from 1.2 to 8 keV.

Similarly, relatively little data are available below 100 eV on the photoelectric absorption coefficients of most filter window materials. A table of optical constants, including absorption coefficients, on some metals from 10 eV to 10 keV was compiled at the Deutsches Elektronen-Synchrotron (DESY).[8] Henke and Ebisu[9] compiled a complete table of absorption coefficients from 100 to 1500 eV, Viegele et al.[10] published a table above 100 eV, and several good tables exist for coefficients above 1 keV.[11,12] To produce a calibrated detection system, it is necessary to survey the photoelectric yield from 25 eV to 10 keV of various potential cathode materials and to measure the filter window photoelectric absorption coefficients in regions where data are unavailable.

In Section II, we describe the XRD's construction and time-response measurements. In Section III, we describe the detector calibration, discuss the results of our cathode quantum efficiency and filter window transmission measurements, and compare our results to a model of total yield.[13] In Section IV, we describe the reproducibility of manufacturing the photocathodes and discuss the effects of aging and the laser fusion experimental environment on the detector sensitivity. In Section V, we show some low-energy x-ray spectra measured on the HELIOS CO_2 laser system at LASL. We also show the results of time-resolved x-ray measurements from 1 to 5 keV taken with the GEMINI CO_2 laser and single- and two-beam Nd-YAG lasers. In Appendix A, we present a compilation of our quantum efficiency measurements; Appendix B contains our measurements of filter window photoelectric mass absorption coefficients.

II. THE DETECTORS

A. Construction

We built XRDs for measuring both time-integrated and time-resolved x-ray spectra. The first type is a miniaturized four-element XRD array in an 11.43-cm Conflat* flange. A picture of this detector with the filter window holder removed is shown in Fig. 3a and a cross section is shown in Fig. 3b. The cathodes are 1.40-cm-diam metal buttons of the desired material mounted on Berkley Nucleonics Corp. (BNC) vacuum feedthrus. The cathodes are biased negatively at 500-1000 V with respect to the anode and the signals are read through a low-inductance dc isolating capacitor. The time response of these detectors is a 600-ps FWHM when measured through 3.05 m of RG 58 cable and the signals are recorded on either a standard 500-MHz laboratory oscilloscope or a fast-gated electronic integrator.

We built the second type of XRD for time response and mounted the single unit on an 11.43-cm Conflat flange. The same type of demountable cathode is used as for the slower version XRD. Because the signals are recorded on 5-GHz bandwidth single-shot oscilloscopes, the time response of the detector should be ≤ 65 ps, the scope risetime. It should also have a well-matched 50-Ω characteristic impedance to suppress reflections. The detector is shown in Fig. 4a and a cross section is shown in Fig. 4b. The anode is biased positively with respect to the cathode to remove any coupling capacitors from the signal line that might limit the system bandwidth. The anode also forms a 15-nf capacitor with the XRD housing to store charge and maintain the anode-cathode gap voltage during the first few hundred picoseconds of the x-ray pulse. We have added a 0.61-m-long, 50-Ω vacuum transmission line behind the anode to allow at least 4 ns before the return of any reflections from the vacuum feedthru. The best vacuum feedthru we have found for these frequencies is a nonvacuum General Radio model 874 connector** sealed with a thin layer of epoxy. Both fast single-pulse and 18-GHz time-domain reflectometer (TDR) measurements show that the reflected pulse at the feedthru is less than 3% of the main pulse.

B. Time Response

The detector risetime t_r, in seconds, is given by the electron flight time across the anode-cathode gap spacing d in meters (Ref. 14):

$$t_r = \frac{d(2m_e/e)^{1/2}}{V^{1/2}} \quad , \qquad (1)$$

where V is the diode bias voltage and m_e and e are the electron mass in kilograms and charge in coulombs, respectively. We assume in this derivation that the electrons have zero initial velocity. The detector's fall time t_d, in seconds, is the decay time of the anode-cathode gap capacitance into the transmission line characteristic impedance R:

$$t_d = R \times 8.05 \times 10^{-12} \frac{A}{d} \quad , \qquad (2)$$

where A is the cathode area in square meters. We chose a detector cathode diameter of 1.39×10^{-2} m, an anode-cathode gap spacing of 1.27×10^{-3} m, a bias voltage of 3 kV, and a 50-Ω characteristic impedance to match the oscilloscope. This gives a 10-90% risetime of 62 ps and an RC decay time constant of 53 ps, which should yield a detector with a FWHM of 73 ps.

To measure the risetime of the detector, we irradiated an aluminum slab target with a 1.2-j, 30-ps mode-locked Nd-YAG laser and measured the time history of low-energy x rays. The XRD used an aluminum cathode with a Kimfoil window that gave a peak response just below the carbon K absorption edge at 284 eV. A typical trace for 3-kV detector bias and 1.27-mm anode-cathode gap spacing is shown in Fig. 5 as recorded on a 5-GHz TMC-4 oscilloscope.[15] This oscilloscope uses a cathode ray tube (CRT) built by the French Philips Company, with an electronics package built and designed at LASL. Figure 6 shows how the 10-90% risetime varies with detector voltage and anode-cathode gap separation. The data follow the $V^{-1/2}$ dependence of Eq. (1) to within the statistics of the data for both anode-cathode gap spacings after deconvolving the 66-ps risetime of the scope. However, the minimum 50-ps risetime is significantly shorter than the expected 62 ps. This may be due to a smaller anode-cathode gap spacing than desired or may result in part from the nonzero initial veolocity of the no-loss primary and Auger photoelectrons emitted from

---

*Conflat is a registered trademark of Varian Associates.

**Manufactured by General Radio Corporation.

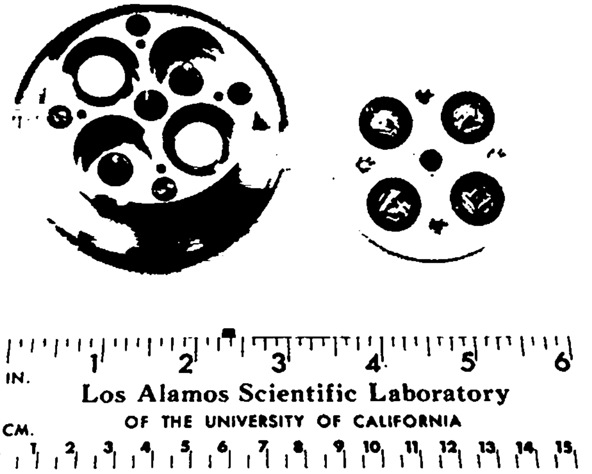

Fig. 3a.
The four-element XRD array with the filter window holder removed.

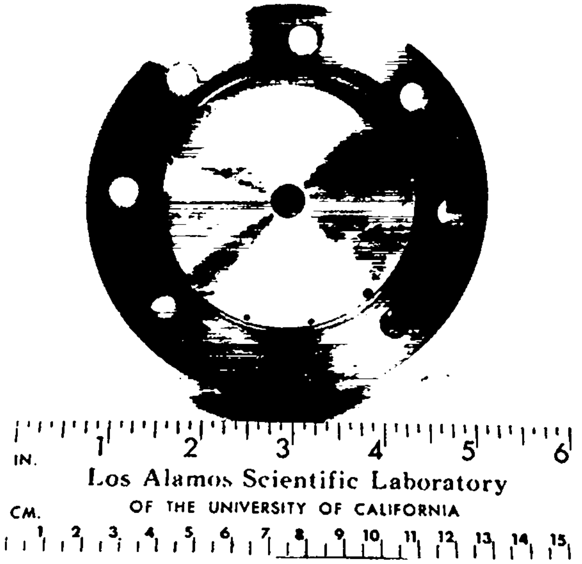

Fig. 4a.
The 5-GHz XRD.

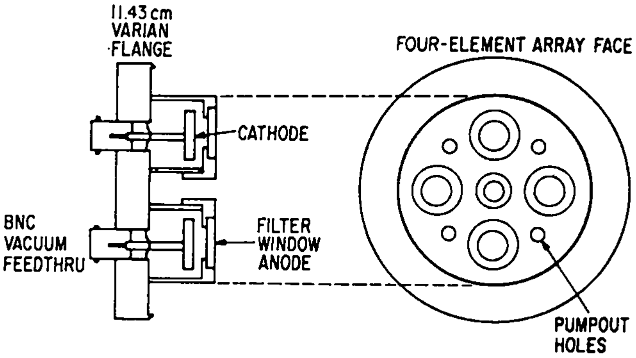

Fig. 3b.
Cross section of the four-element XRD array.

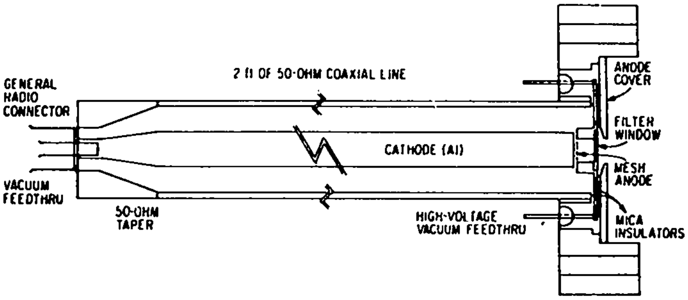

Fig. 4b.
Cross section of the 5-GHz XRD.

the photocathode. When we use the 50-ps measured risetime and the expected 53-ps RC decay time constants, the detector has a FWHM response time of 65 ps.

To date, we have not directly measured the fall time of the detector, as x-ray sources with sufficient intensity and rapid turn off have not been available. The thermal decay of the low-energy x rays in the laser-induced plasma is much longer than the expected fall time of the detector (Fig. 5). In the near future, we will use the 40-ps electron beam pulse from the EG&G, Santa Barbara Linac to generate a Cerenkov light pulse that we hope to measure with a vacuum ultraviolet (VUV) sensitive cesium iodide photocathode. This should give us our first measure of a rapidly falling signal.

III. THE CALIBRATION

To make a useful detector system, it is necessary to measure the quantum efficiency of potential photocathodes from 20 eV to 10 keV and to measure the transmission of our filter windows below 100 eV. We have not attempted to prepare photocathodes of the highest purity and cleanliness; rather, like Cairns and Samson,[4] our cathodes are commercially available "high purity," >99%, samples that have been dry machined to at least a 64 finish and routinely cleaned in freon and ethanol. The cesium iodide, scandium, and evaporated carbon surfaces were subsequently prepared by vacuum evaporation. Because cesium iodide is deliquescent, these

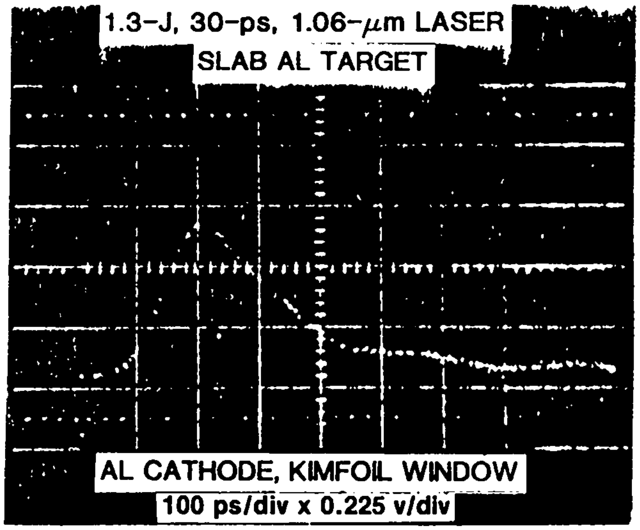

Fig. 5.
An oscilloscope trace showing the fast XRD risetime.

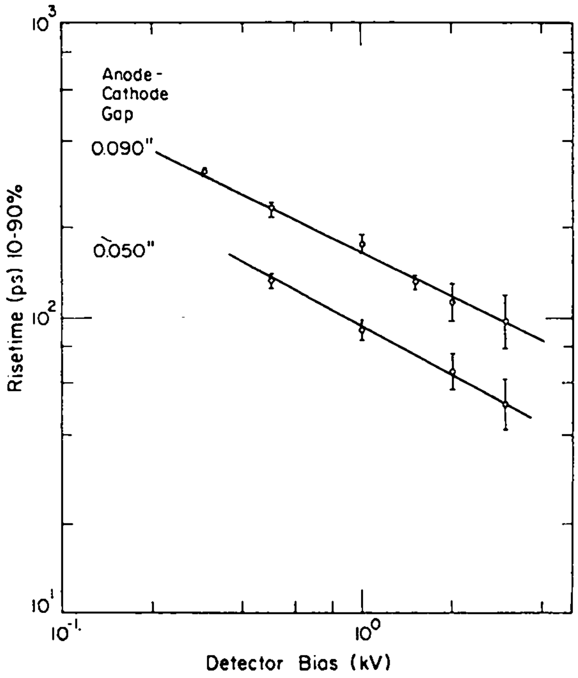

Fig. 6.
XRD risetime vs anode-cathode gap voltage and anode-cathode spacing.

surfaces are heat sealed in plastic bags under dry nitrogen and stored in a desiccator. Our primary interest is not to characterize elemental surfaces, but to prepare "practical" photocathodes that can be manufactured and reproduced easily and remain stable during experiments lasting up to several weeks.

We used three x-ray sources to cover the energy range from 25 eV to 10 keV. The region from 25 to 250 eV was measured at the synchrotron ultraviolet radiation facility (SURF II) of the National Bureau of Standards (NBS). The region from 1 to 10 keV was measured with a fluorescent x-ray source at the LASL soft x-ray calibration facility, whereas the range from 250 eV to 1 keV was covered with an ultrasoft interchangeable anode x-ray source at the LASL soft x-ray calibration facility. Though each source has been described in detail elsewhere,[16-18] we briefly describe how the experiment was performed at each facility.

A. SURF II

The SURF II facility is an 83.8-cm-radius electron storage ring with a maximum beam energy of 250 MeV. As shown in Fig. 7, the radiation from the machine is dispersed by a toroidal grating monochromator with 2-Å resolution and the dispersed beam passes through a 5-mm-diam aperture striking the photocathode. Data are taken in two energy regions. The first is from 25 to 76 eV with a thin aluminum window to postfilter the beam and suppress second-order reflected photons. In this energy region, data are taken with electron beam energies of 140 and 250 MeV. The two beam energies allow us to correct accurately for second-order and scattered photons across the entire energy range. The second energy region is from 76 to 248 eV using a thin polypropylene postfilter and a 250-MeV electron beam. The cathodes are mounted in an NBS-designed diode with a cylindrical anode as shown in Fig. 8. The guard ring shown in this figure was a modification used at LASL to reduce the anode leakage current. The photoelectric currents are measured with a vibrating reed electrometer and the data are reduced on-line by a microcomputer-controlled data acquisition system. Absolute dosimetry is performed with a noble gas double ionization chamber[18] that is an integral part of the vacuum chamber.

The rear of the sample chamber is pictured in Fig. 9. The beam line is inclined with respect to the floor of the experimental hall and the synchrotron is 11 m in front of the chamber. The front handles hold the filters while the rear handles manipulate the diodes. Up to five cathodes and four filters can be measured in a single load.

The window material's photoelectric absorption coefficients are measured by inserting a filter in front of a

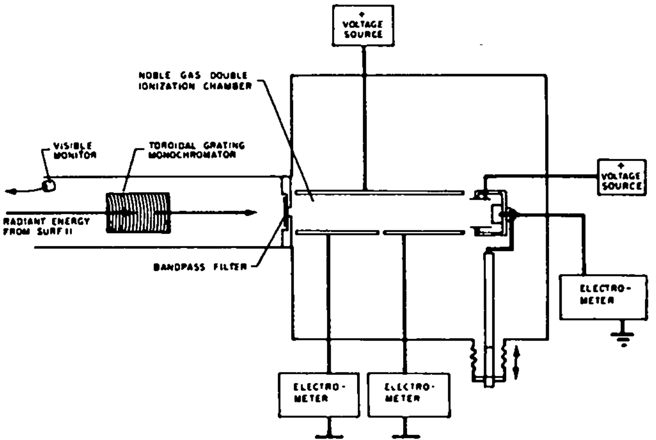

Fig. 7.
The X-ray ultraviolet (XUV) calibration beam line at the NBS SURF II radiation source.

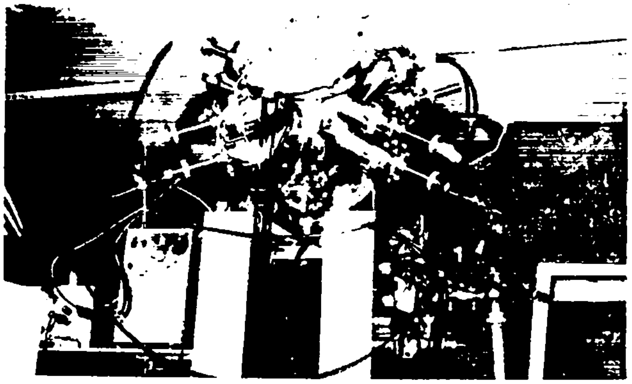

Fig. 9.
The end of the XUV calibration beam line at SURF II.

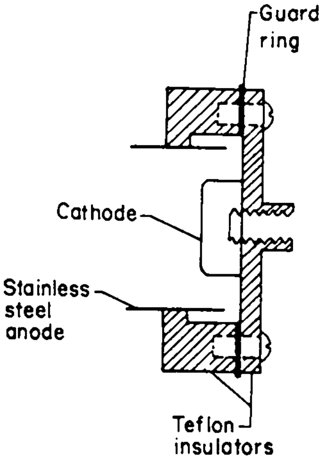

Fig. 8.
Cross section of the NBS cathode holder.

standard aluminum photocathode. By comparing measured diode currents with the filter in and the filter out, the filter transmission is measured directly; and from the known thickness of the filter window, it is possible to determine its x-ray mass-absorption coefficient. The filters are biased positively with respect to the diode to collect any stray electrons emitted from the filter. A lower limit of 1% transmission is measurable, with the limit set by the noise inherent in the cables that connect the diode to the electrometer.

B. The LASL X-Ray Facility

The x-ray region from 250 eV to 10 keV is covered by two x-ray sources. The lower energy region from 250 eV to 1.5 keV is covered by the ultrasoft x-ray source shown in Fig. 10. The x-ray anodes are interchangeable to vary the characteristic line emission from the source and the detectors view the x-ray anodes directly. Source purity is controlled by postfiltration and maintaining low electron accelerating potentials. Dosimetry is performed with a flow proportional counter and the photocathode currents are measured with a vibrating reed electrometer and recorded digitally through a voltage-to-frequency converter. The energy region from 1.5 to 10.5 keV is covered with a fluorescent x-ray source (Fig. 11). A "Henke" x-ray tube is used to fluoresce various characteristic x-ray lines. Purity is controlled by varying the x-ray tube voltage and postifiltration of the fluorescent beam. Dosimetry is performed with a xenon ionization chamber run at atmospheric pressure.[20] The photocathode currents are recorded in the same manner as for the ultrasoft x-ray source.

In both systems, six diodes are mounted linearly in a slider that moves so that any of the cathodes will intercept the x-ray beam. A series of apertures and a thin filter window are used to intercept stray electrons. The cylindrical anode is maintained at + 50 V. A separate shield electrode with an aperture that defines the x-ray beam is maintained at + 200 V (Fig. 12). The horizontal tube contains the array of cathodes and the

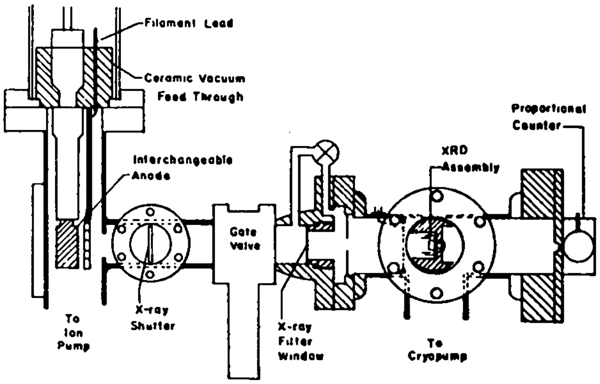

Fig. 10.
The LASL ultrasoft x-ray source.

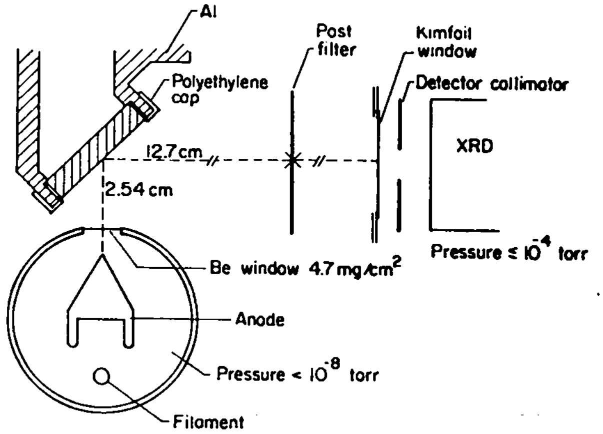

Fig. 11.
The LASL fluorescent x-ray source.

x-ray source and filter wheel are to the left. The ionization chamber is mounted just behind the cathodes to allow frequent dosimetry, and the data acquisition system can be seen in the background.

At the LASL and NBS facilities, the relative error of the measured currents is >2%. The errors on the measured quantum efficiencies of ±10% are determined by the estimate of systematic errors from absolute dosimetry, beam stability, beam purity, and geometry.

C. The Quantum Efficiencies

The quantum efficiencies are compiled in Appendix A. Samples of aluminum, nickel, copper, chromium, 1000 Å of gold evaporated on copper, 1000 Å of carbon evaporated on copper, vitreous carbon, and vitreous carbon that was lightly abraded with sandpaper were measured over the entire energy range. We measured quantum efficiencies for 1000 Å of cesium iodide evaporated on aluminum and 1000 Å of scandium evaporated on aluminum from 1.5 to 10.5 keV. All of these measurements, except the titanium L_α (452 eV), oxygen K_α (525 eV), iron LA(705 eV), and copper L_α (930 eV), were made within a few weeks of each other in January and February of 1978 and represent the quantum efficiencies of recently manufactured surfaces as described at the beginning of Section III. The titanium, oxygen, iron, and copper points were measured from March to April, 1978.

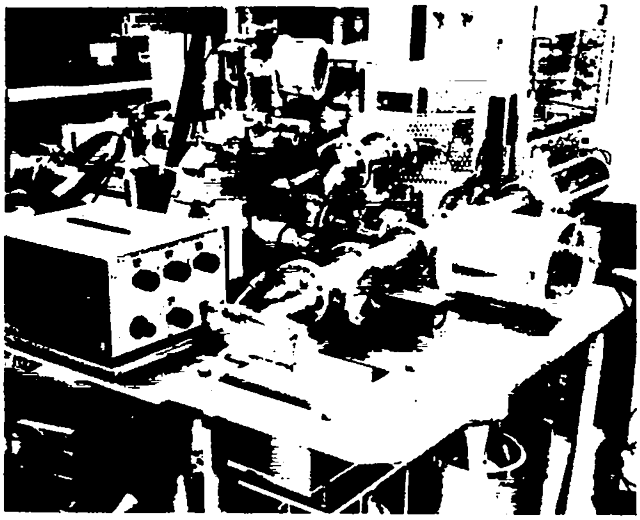

Fig. 12.
The LASL fluorescent x-ray source and data acquisition system.

In Section IV, we quantitatively compare our results to Henke's model of total yield.[13] However, here we merely note that in this model, total yield is proportional to $\mu(E)*E$, where $\mu(E)$ is the energy-dependent mass absorption coefficient. The quantum efficiencies shown in Appendix A follow this trend. The absorption edges of most materials are clearly visible. In addition, we see large discontinuities between the carbon K_α data point at 277 eV and the iron L_α point at 705 eV. This indicates that there are significant surface layers of carbon, nitrogen, or oxygen. The presence of such surface layers is not unexpected as we took no special precautions to suppress them during surface preparation and use. However, uncertainty in the exact cathode quantum efficiency in this region does not introduce serious uncertainty in the response of our detectors, because the filter windows are chosen to strongly attenuate x rays between the carbon and oxygen absorption edges.

An anomaly in the data is the unusually high quantum efficiency at carbon K_α (277 eV) on the carbon cathodes; whereas, on the aluminum, nickel, copper, and gold data, the carbon data points match a continuation of the data from below to within the limits of error. The anomolously high response for carbon probably results from an overlap of the emission spectrum of the x-ray source with the low-energy side of the carbon absorption feature, which results in enhanced photon deposition and increased yield.

This reasoning also argues against carbon being the dominant surface contaminant that gives rise to the large jumps in the quantum efficiency of the aluminum, nickel, copper, and gold data between the carbon data point and the iron L_α data point. If a carbon surface layer were the major contaminant, we would expect the same enhancement of the carbon K_α data points as seen on carbon cathodes. Therefore, in the response curve for aluminum cathode XRDs of Fig. 2, we show all the jump at the oxygen edge.

The evaporated cesium iodide surface is a particularly interesting cathode because its quantum efficiency is two orders of magnitude larger than aluminum and 30 times larger than gold from 1 to 10 keV. X-ray intensity from laser fusion plasmas typically fall very rapidly through this region and the low quantum efficiency of metallic photocathodes make spectra immeasurable. We can record signals in this energy region with cesium iodide and will demonstrate some typical results in Section V.

D. The Filter Window Absorption Coefficients

In Appendix B, we compiled the photoelectric mass absorption coefficients for our filter windows. The samples were 7660 Å of rolled aluminum, 272 $\mu g/cm^2$ of Kimfoil with a 400-Å aluminum surface layer, 70 $\mu g/cm^2$ of polypropylene with a 50-Å nickel-chromium surface layer, and 33 $\mu g/cm^2$ of Formvar. We measured two samples of each material. With the Kimfoil and polypropylene samples, we divided out the transmissivity of the metallic surface layers. The solid lines on the curves are the published coefficients of Henke and Ebisu.[9] For aluminum below 100 eV, we used the DESY data.[8] We also measured samples of 5000-Å, vacuum-evaporated aluminum; however, we could not reliably remove the backing material and we have not used this type of window.

In general, the agreement between published absorption coefficients and out data is quite good. One exception is aluminum below the aluminum $L_{2,3}$ absorption edge where the coefficients are anomolously high for low transmissions and low for high transmissions. This may result from nonuniformities in our rolled foils or inconsistencies with the published data. However, these curves represent the best transmission data of the filters we actually use; and these measurements were employed in generating the response curves shown in Fig. 2.

E. Experiment and Model Comparison

Henke et al. proposed a model of photoyield[13] where the electron yield per photon Q(E) for incident photons of energy E is

$$QE \ \alpha \ \mu(E) \times E \times f(E) \text{ (electrons/photon)}, \qquad (3)$$

where $\mu(E) \times E$ is the photon energy deposition per unit distance near the surface of the cathode and f(E) is a slowly varying function of energy related to the efficiency of converting photo and Auger electron energy into secondary electrons.

To test this result, we plotted $Q(E)/\mu(E)^*E$ vs E in Fig. 13 for the unabraded vitreous carbon, gold, and aluminum samples. The resultant curve is the energy dependence of f(E). The lines drawn through the data points of Fig. 13 are provided to guide the eye and do not represent a model of f(E).

In general, f(E) is a slowly varying function of energy and the term $\mu(E)^*E$ accounts for most of the two or three orders of magnitude variation in quantum efficiency. For gold, f(E) does not vary by more than 20-30% from 20 eV to 10 KeV. A small anomaly is seen near 150 eV at the N absorption feature and again at 1.8 keV at the M absorption edge. Aluminum shows the largest variation with a distinct jump at the aluminum K absorption edge and large changes in f(E) over the entire range of energies. The aluminum surface was modeled as Al_2O_3, and if we use a pure aluminum surface, the effect is even more pronounced. For the carbon surface, f(E) is again slowly varying except at very low energies and with a 30% decrease from 100 eV to 1.5 keV.

IV. REPRODUCIBILITY AND AGING

A. Reproducibility

To avoid extensive calibration of every surface to be used in an experiment, we would like a technique for

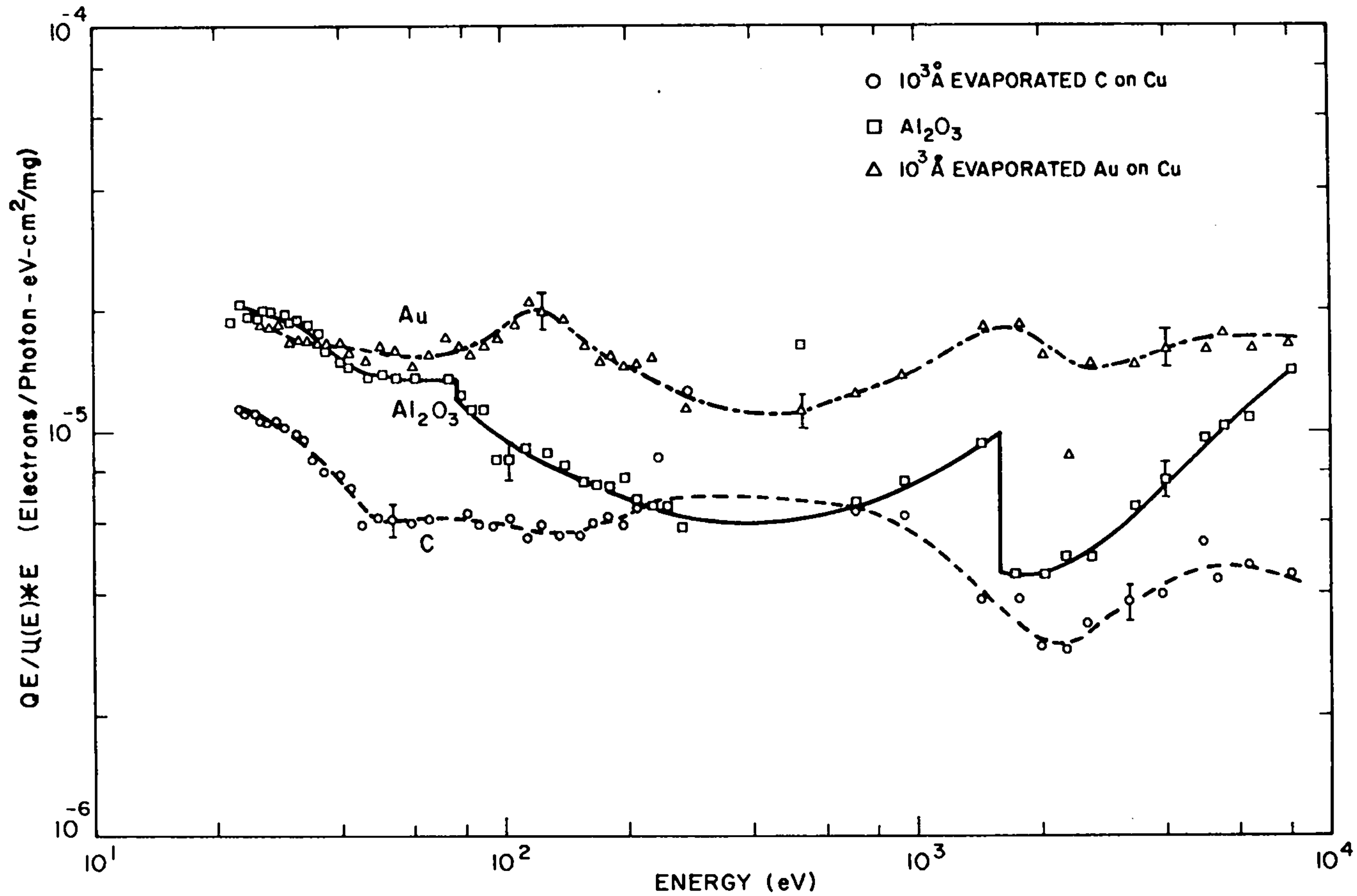

Fig. 13.
Energy dependence of f(E) (see text) vs energy for Al_2O_3, gold, and carbon.

producing surfaces with the same initial quantum efficiency. To test the reproducibility of our manufacturing technique, we prepared a set of five identical samples of 1100 series (>99% pure) aluminum cathodes and calibrated them at C K_α. The samples were prepared in the usual way by dry machining the bulk material and cleaning with freon and ethanol. The results are shown in Table I, where the mean preshot quantum efficiency is 0.0267 ± 0.0025. This indicates that samples prepared from a single supply of material by a standard method will give reproducible quantum efficiencies to better than ±10%. Also, a sixth cathode of 1100 series aluminum produced from a different bulk sample had a quantum efficiency of 0.0294, which is within one standard deviation of the other samples.

We also produced two identical samples each of aluminum, nickel, copper, evaporated gold, and evaporated carbon, and calibrated them from 25 to 250 eV; their quantum efficiencies were identical to better than ±10% across this entire range. Thus, it is possible to produce samples with identical quantum efficiencies to ±10% by a simple standardized procedure.

B. Effects of the Laser Fusion Environment

We would like the detector sensitivity to remain unchanged in the environment where it will be used, and to be stable during a few weeks of experimentation. To test the effects of the laser fusion experimental environment, we prepared a set of five identical 1100 series aluminum cathodes with 272-μg/cm² Kimfoil windows and one 6061 series aluminum alloy cathode. We then exposed these diodes to different numbers of laser shots with the cathodes remaining on the target chamber up to 2 wk. After 2 wk, all diodes were calibrated. The average sensitivity decreased by 6.6%, but there was no systematic effect related to time spent in the laser target chamber or number of target shots. Therefore, during the 2 wk and up to 10 target shots, we saw no effect

TABLE I

THE CHANGE IN SENSITIVITY OF ALUMINUM CATHODES AS A FUNCTION OF THE NUMBER OF TARGET SHOTS. CALIBRATION IS AT 277eV (C Kα).

Cathode No.	Material (Al)	No. of Shots	Preshot Calibration (Quantum Efficiency)	Postshot Calibration (Quantum Efficiency)
1	6061-T6	Control	0.025	0.023
2	1100-H14	Control	0.028	0.027
3	1100-H14	0[a]	0.027	0.025
4	1100-H14	1	0.024	0.022
5	1100-H14	3	0.025	0.024
6	1100-H14	10	0.030	0.028

---

[a] Pumped out with the laser chamber.

that can be ascribed to the laser fusion experimental environment.

This does not mean, however, that cathodes can be prepared and used for long periods of time without significant changes in sensitivity. We merely have established that we can produce surfaces with quantum efficiencies that are identical to ±10% that can be used for short periods of time with less than 10% change in absolute sensitivity.

We also monitored the condition of the filter windows. Although laser target shots deposit insufficient material to significantly alter the filter window transmissivity, the hot plasma and occasional pieces of shrapnel can degrade the filters. Therefore, it is necessary to inspect the filter windows frequently and change them at least as often as the cathodes.

C. Effects of Cathode Aging

We monitored the long-term change in cathode sensitivity by recalibration of the aluminum, evaporated gold, and evaporated carbon samples over the following year. The initial set of cathode surfaces described in Section III.C. were first calibrated during January through February 1978 and used in a laser fusion experiment in May when each detector was exposed to six shots of the GEMINI CO_2 laser-irradiating neon-filled glass microballoons.

We also maintained control samples of the aluminum, evaporated gold, and evaporated carbon surfaces at NBS. Here we discuss the effects of long-term aging on the control cathodes and then relate these results to the changes seen on the cathodes that were used at LASL.

We recalibrated the quantum efficiencies of all surfaces from 75 to 250 eV in July of 1978. The control samples of aluminum and evaporated carbon were maintained in the sample chamber at 10^{-8} torr during the interim and their efficiencies were unchanged from 75 to 250 eV as shown in Figs. 14a and b. The data points for the January 1978 calibration are represented as circles and the crosses are the July calibration. Thus, these surfaces do remain stable when maintained in a high-purity ultrahigh vacuum system. On the other hand, the gold cathode shown in Fig. 14c was left in ambient air during this time and shows significant change in quantum efficiency from 75 to 250 eV. In particular, the size of the N absorption feature at 200 eV has been suppressed.

Because of experimental exigencies, it was not possible to finish the recalibration of all surfaces from 25 to 75 eV until December 1978. During the interim, all samples were left out of the vacuum system at NBS. These data from 25 to 75 eV are also plotted in Figs. 14a, b, and c. The carbon surface, which had been stable while in the vacuum system, now changed. The gold surface also shows significant change from its January 1978 calibration. However, we do not see a significant discontinuity at 75 eV between the July and December calibrations. This may indicate that the additional change in the gold surface in the second 6 months was small compared to the first 6 months. The aluminum surface did not show

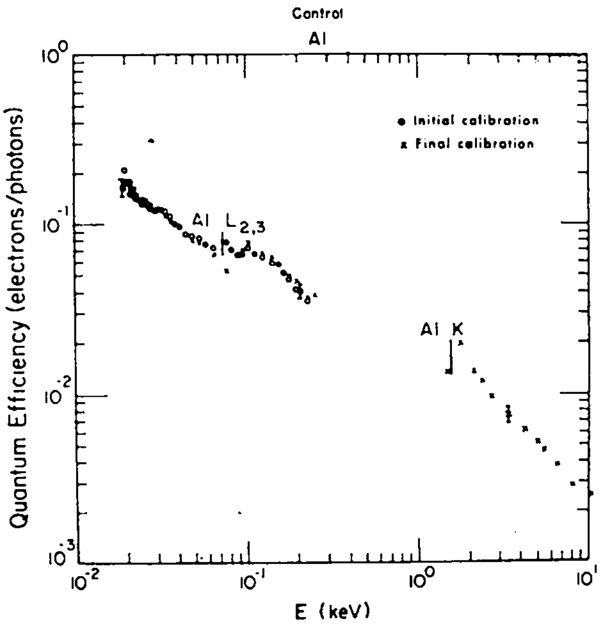

Fig. 14a.
Initial and final calibration of the control aluminum sample.

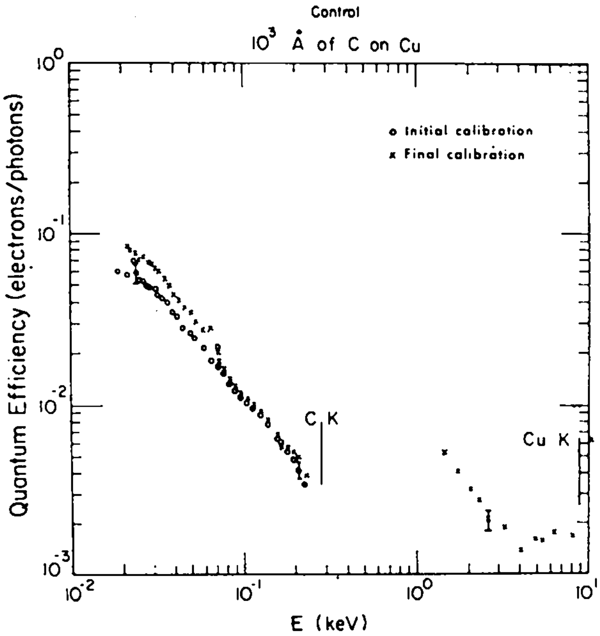

Fig. 14b.
Initial and final calibration of the control evaporated carbon sample.

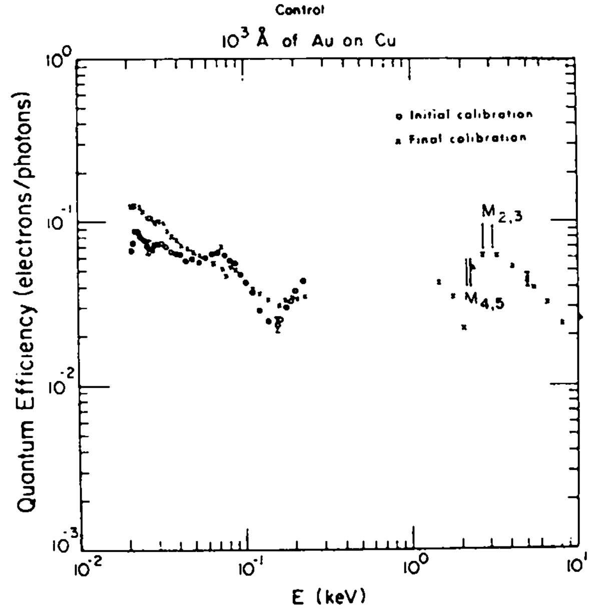

Fig. 14c.
Initial and final calibration of the control evaporated gold sample.

significant changes from January to December 1978. Thus, the control aluminum surface appears to have quickly achieved a stable surface layer after manufacturing and did not change appreciably thereafter.

The aluminum, evaporated gold, and all the carbon samples that were returned to LASL in January 1978 were recalibrated from 25 to 250 eV with the control samples, and all samples were calibrated from 1 to 10 keV in March 1979. The samples that were used at LASL all showed changes in their quantum efficiency by as much as a factor of 2 or 3, except for abraded vitreous carbon, which remained essentially unchanged. These results are plotted in Figs. 15a through e. As with the evaporated carbon control sample, the evaporated carbon sample used at LASL also increased in quantum efficiency. The same is true of the two evaporated gold samples. The aluminum sample that was used at LASL showed a decrease of 50% in sensitivity. The unabraded vitreous carbon sample showed a large increased quantum efficiency, although the abraded vitreous carbon sample did not change. Indeed, all the surfaces changed

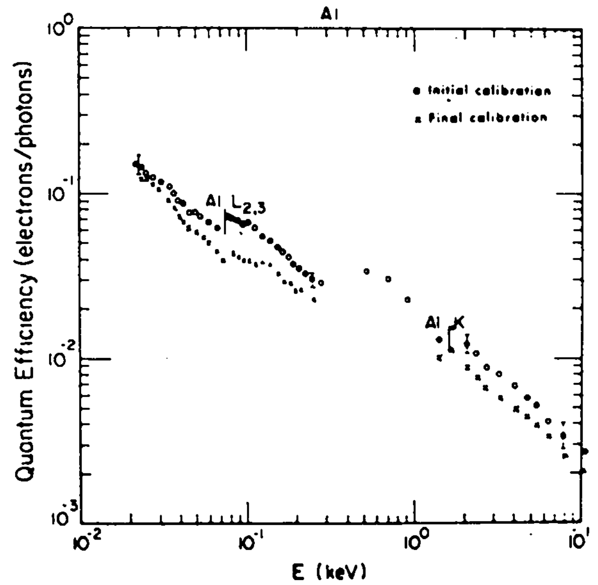

Fig. 15a.
Initial and final calibration of the aluminum sample used at LASL.

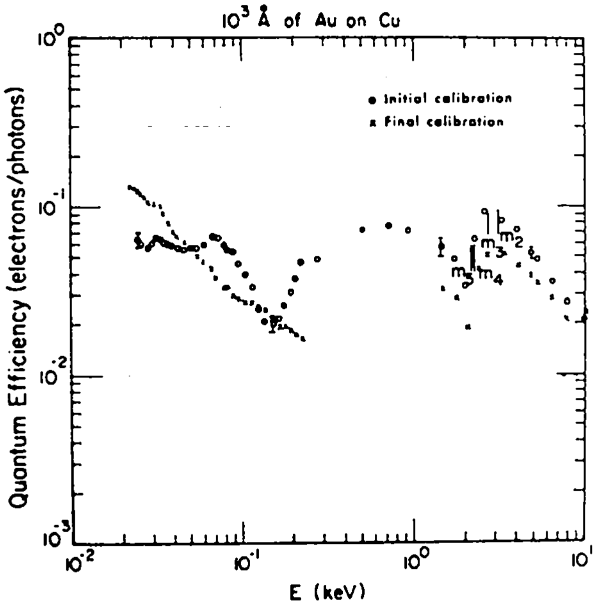

Fig. 15b.
Initial and final calibration of the evaporated gold sample used at LASL.

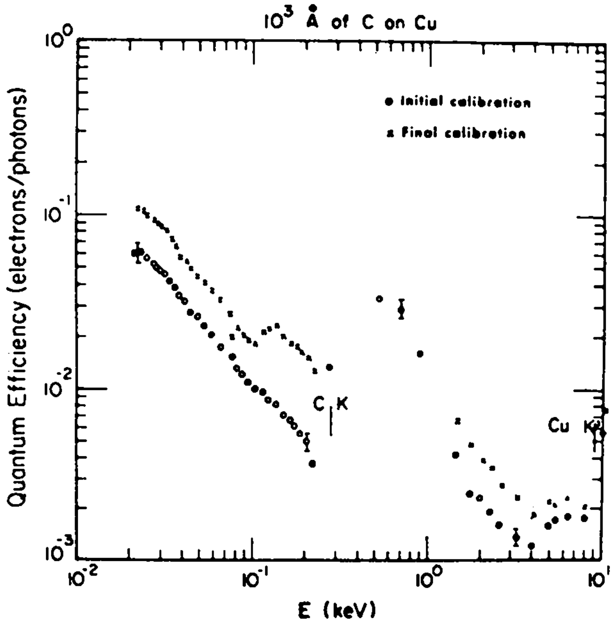

Fig. 15c.
Initial and final calibration of the evaporated carbon sample used at LASL.

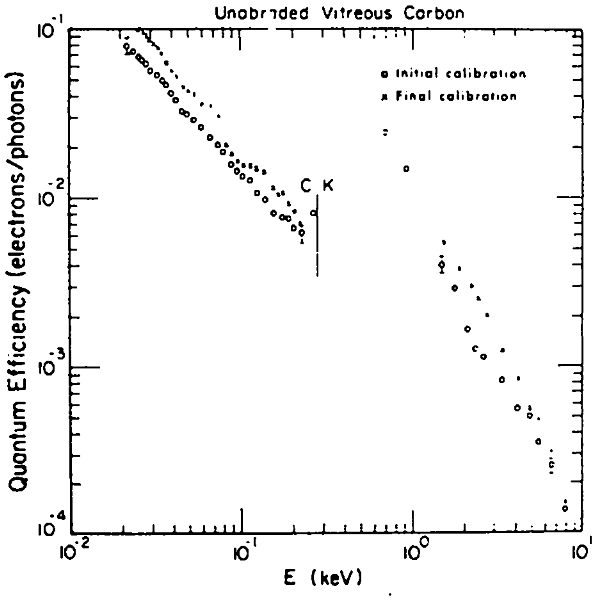

Fig. 15d.
Initial and final calibration of the unabraded vitreous carbon sample used at LASL.

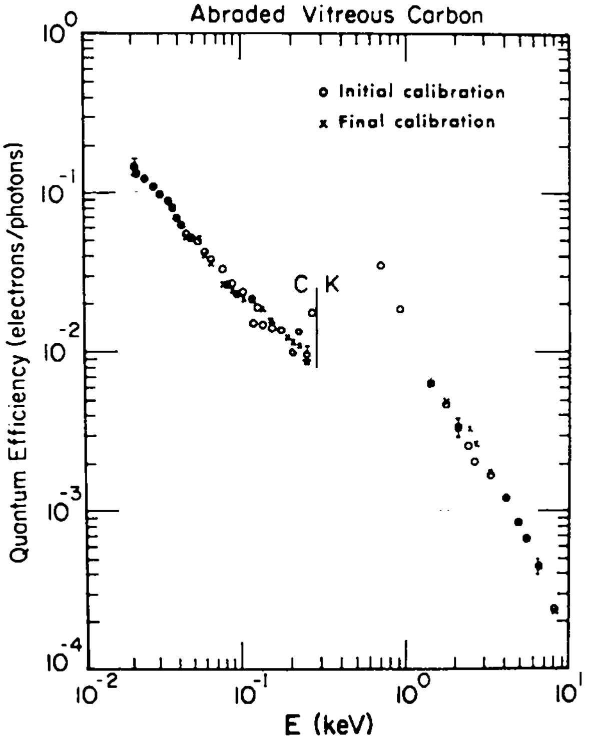

Fig. 15c.
Initial and final calibration of the abraded vitreous carbon sample used at LASL.

so that they exhibit fewer features associated with the characteristic cathode material and tend toward a median quantum efficiency.

We conclude from this study that the aging of the cathode surfaces is a complicated time-dependent process with time constants of months and quantum efficiency changes of a factor of 2 or 3, depending on the surface type and the photon energy. However, based upon the results of Section IV, it does appear possible to prepare identical aluminum surfaces to ±10% that can be used for short periods of time in the laser fusion environment with less than ±15% uncertainty in the absolute detector response. However, to measure absolute fluxes with XRDs, one must be extremely careful to either change cathodes and windows frequently or to recalibrate. Alternatively, based upon the stable response of the control sampes when they are left in an ultrahigh vacuum environment, it may be possible to build stable detectors with small integral pumps and a gate valve to maintain the surfaces in a clean environment except during a shot. This suggestion will be the subject of further study.

V. APPLICATIONS

A. Time-Integrated Ultrasoft X-Ray Spectra

We used the miniaturized four-element XRD array discussed in Section II to measure time-integrated ultrasoft x-ray spectra for 200-µm-diam D-T filled glass microballoons imploded with the LASL eight-beam CO_2 laser, HELIOS. Typical total beam energies and powers for these shots are 4 kJ at 4 TW. The XRD channels all used aluminum cathodes with windows of 7600-Å aluminum, 272-µg/cm^2 Kimfoil + 400-Å aluminum, 7600-Å aluminum + 1-µm beryllium, and Kimfoil + 2-µm beryllium, which yielded peak sensitivities at 30-70, 277, 750 eV, and 1 keV, respectively. The spectra were then generated by dividing the total integrated charge by the detector sensitivity and the energy width of the channels. The two low-energy channels were corrected for their high-energy response by subtracting the measured charge in the high-energy channels. This correction was usually less than 20% of the total charge in the low-energy channel. The final spectra were then normalized per joule of incident CO_2 laser energy. The results are plotted in Fig. 16.

It is necessary to provide an electron sweeper in front of the detectors, especially with CO_2 irradiated plasmas. The sweeper will stop the high-energy electrons emitted from the plasma from striking the cathode and causing undershoot in the traces. For our purposes, the sweepers are 1- to 2-kG magnetic fields over a 5-cm-long path apertured to 1-cm diameter at both ends. The interior of the sweeper is lined with a low-Z material to suppress bremsstrahlung. RF-microwave interference is suppressed with grounded wire meshes placed across the sweeper apertures.

B. Time-Resolved X Rays

Figure 17 is a montage of several applications of the fast XRD. The upper left photo shows an x-ray signal taken with an aluminum cathode and Kimfoil window on an aluminum slab target irradiated with a 30-ps, 1.3-J Nd-YAG laser pulse. The signal is recorded with the 5-GHz TMC-4 oscilloscope at 100-ps/div sweep time. The trace demonstrates the risetime of the detector. However, notice the relatively long tail of the trace while the plasma cools. The upper right trace is the same channel recorded on the GEMINI CO_2 laser with a 1-ns laser pulse. The time scale is 1 ns/div and again the x-ray plasma emission lasts much longer than the laser pulse.

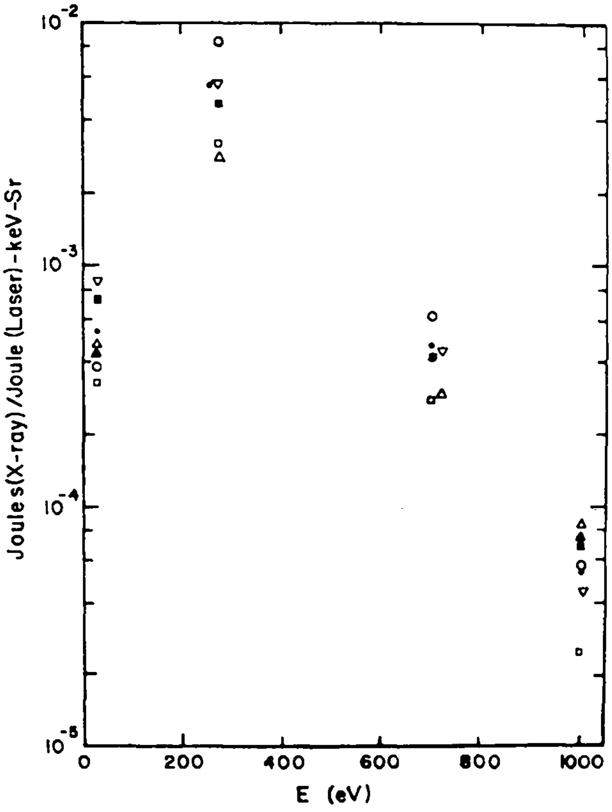

Fig. 16.
Typical x-ray spectra from 200-μm-diam D-T filled glass microballoons imploded with the LASL HELIOS laser.

The lower left-hand picture is a 200-μm-diam, nickel-coated, unfilled glass microballoon imploded with a 0.1-TW, 300-ps, two-beam Nd-YAG laser. The detector utilized a cesium iodide cathode with a 0.92-mg/cm^2 chlorine window + 12 μm of beryllium that gave a peak response at about 1.0 keV. The x-ray pulse at this energy follows the laser pulse much more closely but still appears to have a somewhat extended late-time emission.

The lower right-hand picture was taken with the two-beam GEMINI CO$_2$ laser that irradiated a titanium square 200 μm on a side by 25 μm thick. The detector used a cesium iodide photocathode with an 11.5-mg/cm^2 titanium filter window, which yields a channel with maximum response just below the titanium K absorption edge at 4.5 keV. The x-ray pulse is no wider than the laser pulse at this x-ray energy.

These results are a small sample of the data we have gathered to date. The cesium iodide and other high-sensitivity photocathodes are particularly promising as they allow us to extend the use of these detectors well above 1 keV. Conversely, we can use the increased efficiency of the halide cathodes to recover detector efficiency lost in spatially or energy-dispersive applications. X-ray diodes are very useful tools for measuring time-resolved x-ray spectra. The detector's response is reproducible if cathode preparation is standardized and they can be used for short periods of time in the relatively clean environment of laser fusion experiments without serious changes in sensitivity. However, it is essential that the sensitivity of these detectors be monitored frequently while in use to ensure their absolute calibration.

ACKNOWLEDGEMENTS

We would like to acknowledge the help of Douglas Lier and Thomas Elsberry of LASL in performing many of the calibrations. We also acknowledge Peter Lyons of LASL and Burton Henke of the University of Hawaii for their many useful conservations. Lonnie Hocker of EG&G, Santa Barbara was particularly helpful in the design and characterization of our fast x-ray diode and David Van Hulsteyn of LASL helped in the risetime measurements.

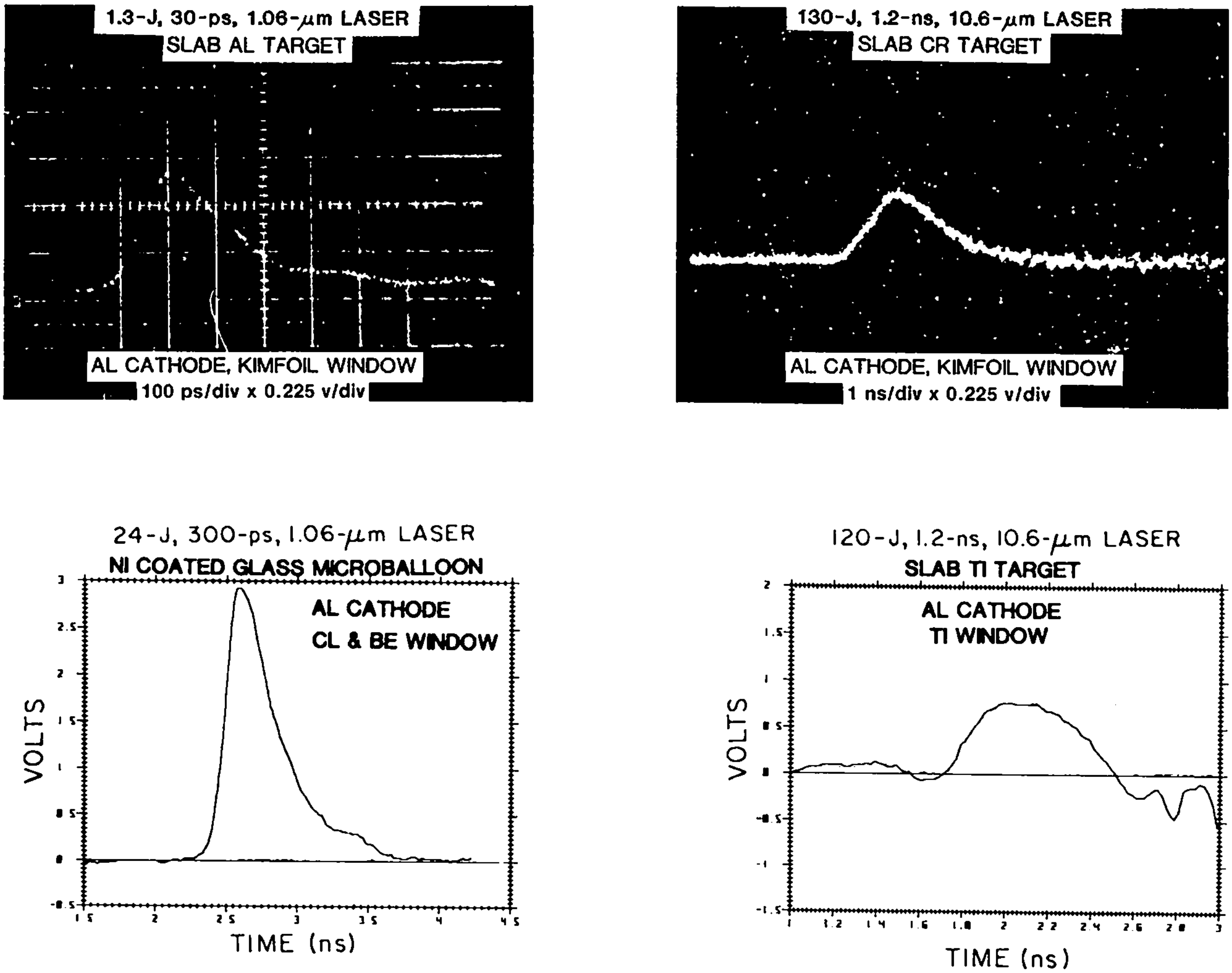

Fig. 17.
Typical time-resolved x-ray pulses.

REFERENCES

1. J. L. Gaines, H. N. Kornblum, and V. M. Slivinksy, "Low Energy X-Ray Detectors for Laser Fusion Targets," Lawrence Livermore Laboratory report UCRL 75987 A (1974).
2. E. J. T. Burns, "Soft X-Ray Vacuum Ultraviolet Diagnostics of High Density, High Temprature Plasmas at the Air Force Weapons Laboratory," Adv. X-Ray Anal. **18** 117 (1974).
3. R. H. Day, "Sub-Kilovolt X-Ray Diode for Laser Fusion Plasma Diagnostics," Bull. Am. Phys. Soc. 22. 1196 (1977).
4. R. B. Cairns and J. A. R. Samson, "Metal Photocathodes as Secondary Standards for Absolute Intensity Measurements in the Vacuum Ultraviolet," J. Opt. Soc. Am. 56, 1568 (1966).
5. E. B. Saloman, "Typical Photoefficiency Between 20-250 eV of Windowless XUV Photodiodes with Tungsten and Anodized Aluminum Oxide Hotocathodes," Appl. Opt. 17, 1489 (1978).
6. J. L. Gaines and R. A. Hansen, "X-Ray Induced Electron Emission from Thin Gold Foils," J of Appl. Phys. 47, 3923 (1976).
7. L. G. Eliseenko, V. N. Schemelev, and M. A. Rumsh, "Quantum Yields of the Surface X-Ray Photoeffect at 1-10 Å," Zh. Tekh. Fiz. 38, 175 (1968), Sov. Physics-Tech. Physics 13, 122 (1968).
8. H. J. Hagemann, W. Gudat, and C. Kunz, "Optical Constants From the Far Infrared to the X-Ray Region: Mg, Al, Cu, Au, Bi, C, and Al_2O_3," Deutches Elektronen-Synchrotron report DESY SR-74/7 (1974).
9. B. L. Henke and E. S. Ebisu, "Low Energy X-Ray and Electron Absorption Within Solids," Adv. X-Ray Anal. 17, 150 (1973).
10. W. J. Viegele, E. Briggs, L. Bates, E. M. Henry, and B. Bracewell, "X-Ray Cross-Section Compilation from 0.1 keV to 1 MeV," Kaman Sciences Corporation report KN-71-431(R) (1971).
11. E. Storm and H. I. Israel, "Photon Cross Sections from 1 keV to 100 MeV for Elements Z = 1 to Z = 100," Nuc. Data Tables 7,565 (1970).
12. W. H. McMaster, N. K. Del Grande, J. H. Mallett, and J. H. Hubbell, "Compilation of X-Ray Cross Sections," Lawrence Livermore Laboratory report UCRL 50174 (1969).
13. B. L. Henke, J. A. Smith, and D. T. Atwood, "0.1-10 keV X-Ray Induced Electron Emissions from Solids—Models and Secondary Electron Measurements," J. Appl. Phys. **48**, 1852 (1977).
14. G. Beck, "Photodiode and Holder with 60-psec Response Time," 77 Rev. Sci. Instrum. **47**, 849 (1976).
15. E. J. McLellan and J. S. Lunsford, "A Single Sweep 5-GHz Oscilloscope-Detector Combination for CO_2 Laser Pulse Measurements," Proc. Conf. Laser Engineering and Applications, Washington, DC (1977).
16. E. B. Saloman and D. L. Ederer, "Absolute Radiometric Calibration of Detectors Between 100-600 Å," Appl. Opt. 14, 1029 (1975).
17. P. B. Lyons and D. W. Lier, "Fabrication and X-Ray Calibration of Thin Plastic Scintillator Detectors," IEEE Trans. on Nuc. Sci. NS- 22, 88 (1975).
18. P. B. Lyons, R. H. Day, D. W. Lier, and T. L. Elsberry, "Sub-keV X-Ray Calibration of Plastic Scintillators," Proc. ERDA X- and gamma-Ray Symp., Ann Arbor, Michigan, paper number 760539, 79 (1979).
19. J. A. R. Samson, "Absolute Intensity Measurements in the Vacuum Ultraviolet," J. Opt. Soc. Am. 54, 6 (1964).
20. P. B. Lyons, J. A. Baran, and J. H. McCrary, "A Total Absorption Ionization Chamber for 1.5-10 keV X-Rays," Nucl. Instrum. Methods 95, 571 (1971).

APPENDIX A
COMPILATION OF QUANTUM EFFICIENCIES

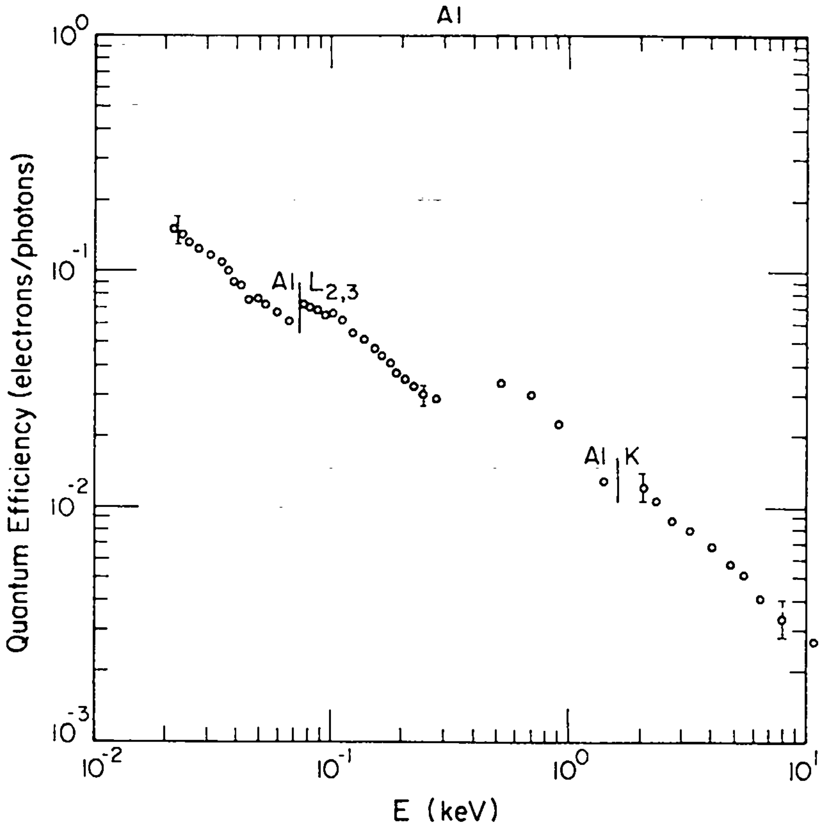

Fig. A-1.
Measured quantum efficiency of aluminum.

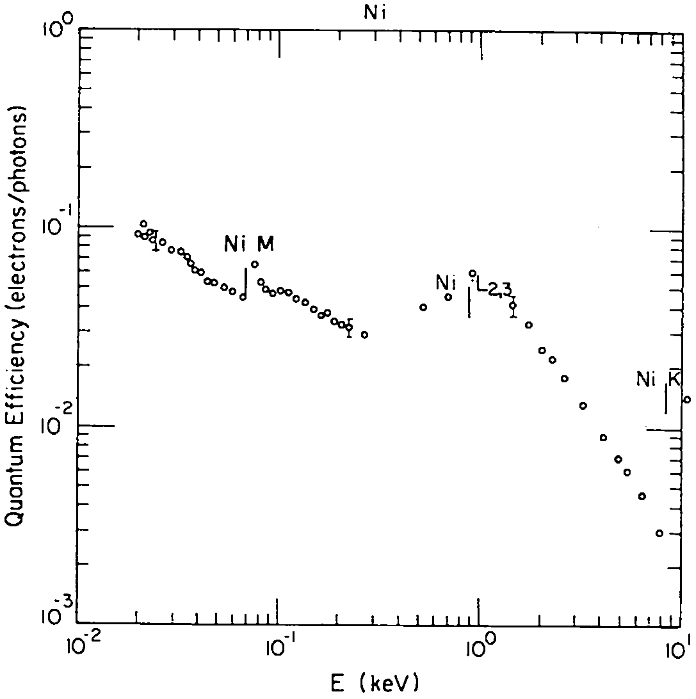

Fig. A-2.
Measured quantum efficiency of nickel.

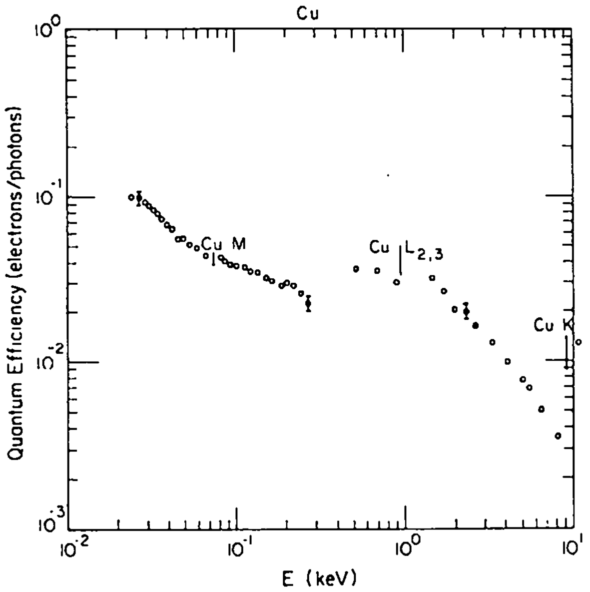

Fig. A-3.
Measured quantum efficiency of copper.

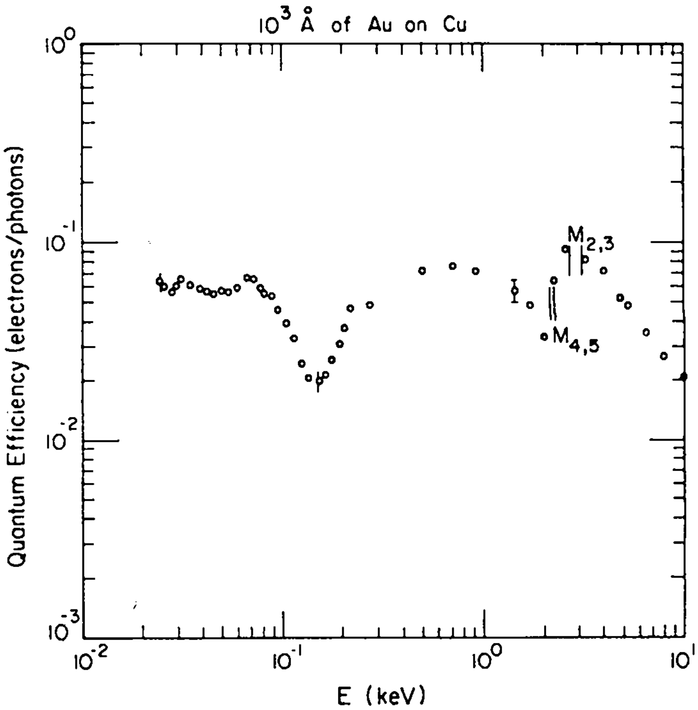

Fig. A-4.
Measured quantum efficiency of evaporated gold on copper.

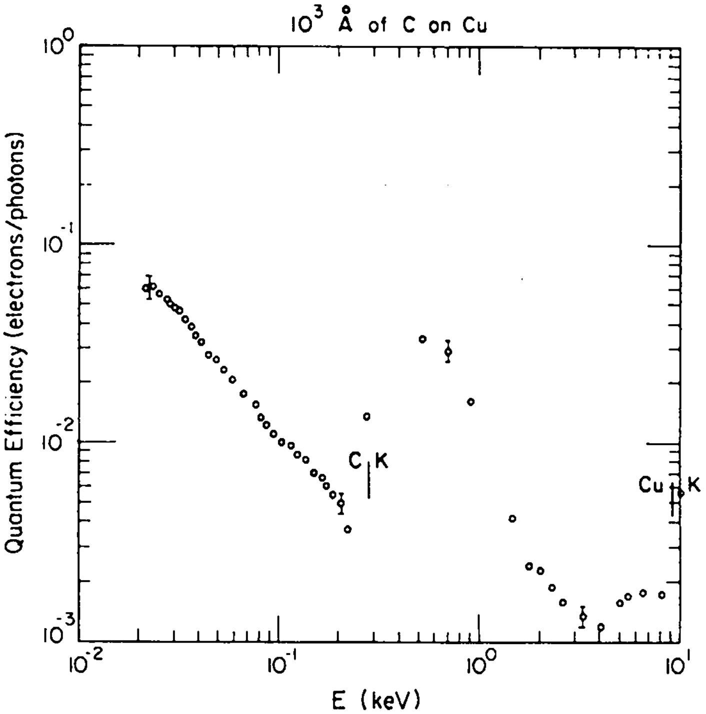

Fig. A-5.
Measured quantum efficiency of evaporated carbon on copper.

Fig. A-6.
Measured quantum efficiency of unabraded vitreous carbon.

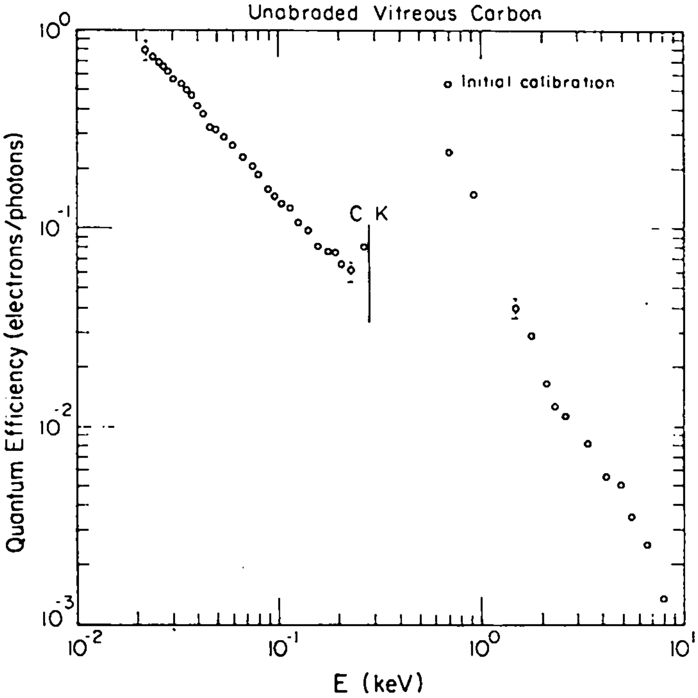

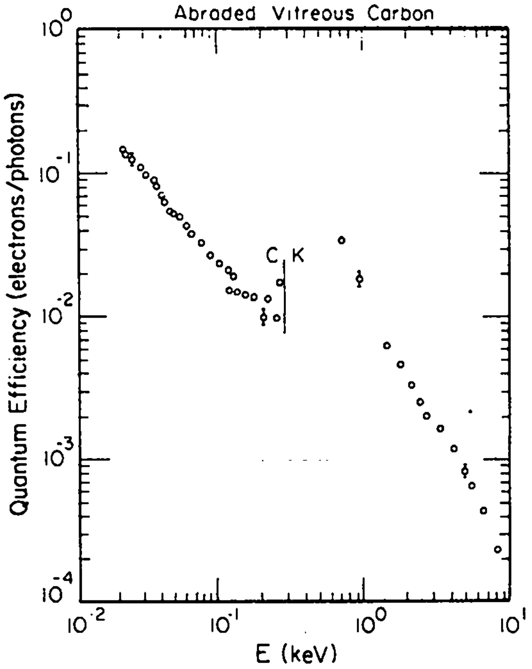

Fig. A-7.
Measured quantum efficiency of abraded vitreous carbon.

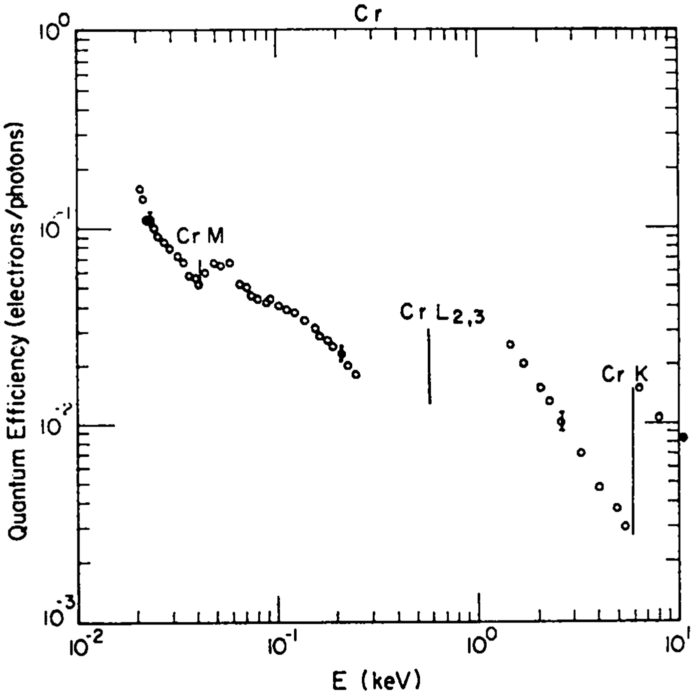

Fig. A-8.
Measured quantum efficiency of chromium.

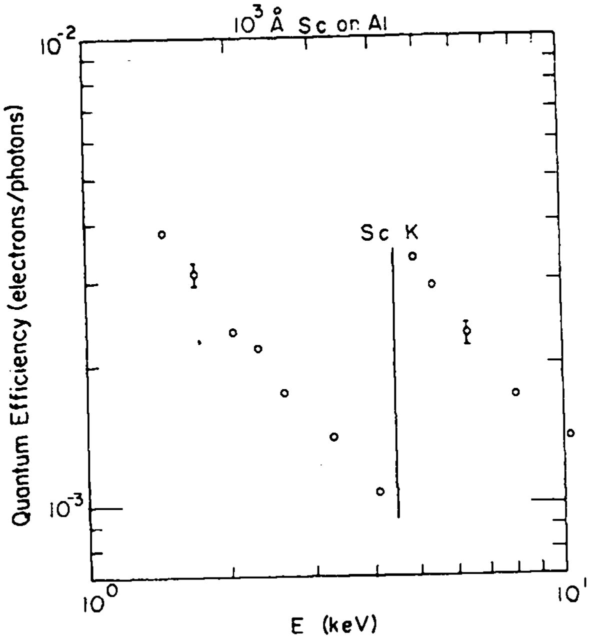

Fig. A-9.
Measured quantum efficiency of evaporated scandium on aluminum.

Fig. A-10.
Measured quantum efficiency of evaporated cesium on aluminum.

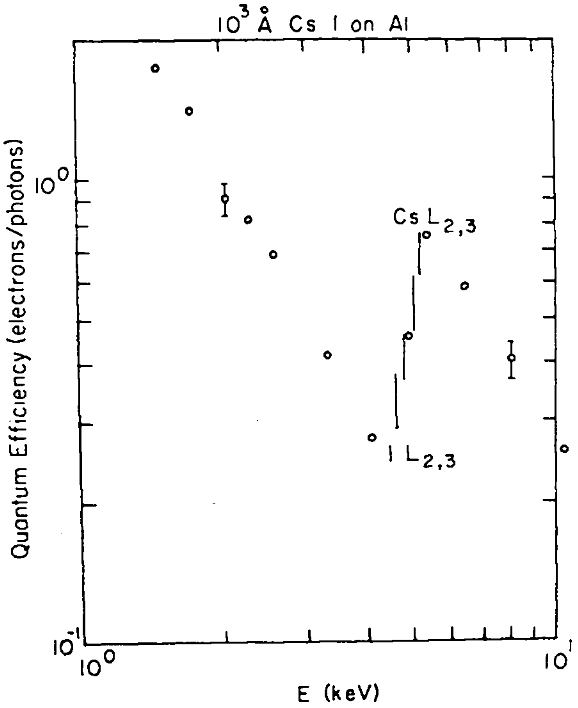

APPENDIX B
COMPILATION OF ABSORPTION COEFFICIENTS

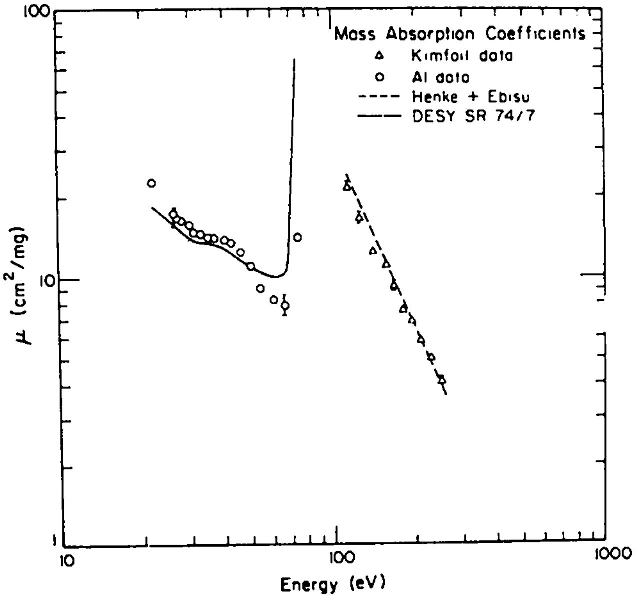

Fig. B-1.
Photoelectric mass absorption coefficients of rolled aluminum and Kimfoil.

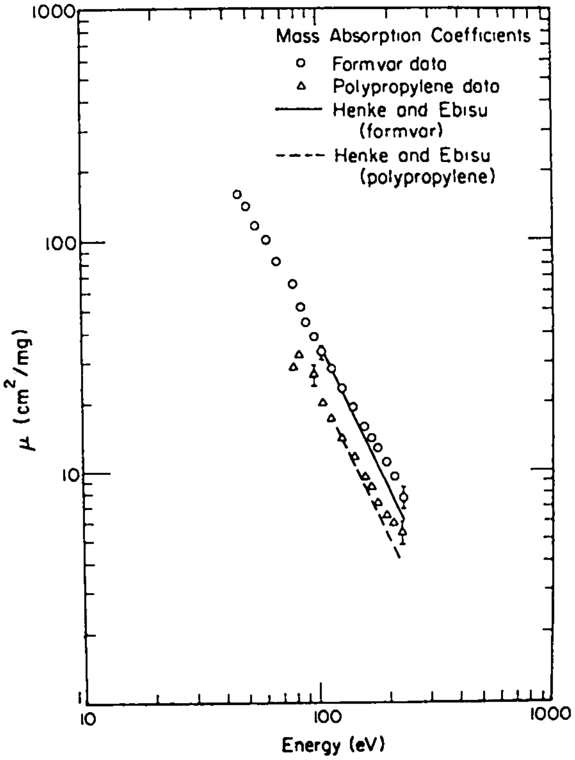

Fig. B-2.
Photoelectric mass absorption coefficients of Formvar and polypropylene.

Printed in the United States of America
Available from
National Technical Information Service
US Department of Commerce
5285 Port Royal Road
Springfield, VA 22161

Microfiche $3.50 (A01)

Page Range	Domestic Price	NTIS Price Code	Page Range	Domestic Price	NTIS Price Code	Page Range	Domestic Price	NTIS Price Code	Page Range	Domestic Price	NTIS Price Code
001-025	$ 5.00	A02	151-175	$11.00	A08	301-325	$17.00	A14	451-475	$23.00	A20
026-050	6.00	A03	176-200	12.00	A09	326-350	18.00	A15	476-500	24.00	A21
051-075	7.00	A04	201-225	13.00	A10	351-375	19.00	A16	501-525	25.00	A22
076-100	8.00	A05	226-250	14.00	A11	376-400	20.00	A17	526-550	26.00	A23
101-125	9.00	A06	251-275	15.00	A12	401-425	21.00	A18	551-575	27.00	A24
126-150	10.00	A07	276-300	16.00	A13	426-450	22.00	A19	576-600	28.00	A25
									601-up	†	A99

†Add $1.00 for each additional 25-page increment or portion thereof from 601 pages up.